Article

Episodic deluges in simulated hothouse climates

https://doi.org/10.1038/s41586-021-03919-z

Received: 21 April 2021

Accepted: 16 August 2021

Published online: 3 November 2021

Check for updates

Jacob T. Seeley[1]✉ & Robin D. Wordsworth[1,2]

Earth's distant past and potentially its future include extremely warm 'hothouse'[1] climate states, but little is known about how the atmosphere behaves in such states. One distinguishing characteristic of hothouse climates is that they feature lower-tropospheric radiative heating, rather than cooling, due to the closing of the water vapour infrared window regions[2]. Previous work has suggested that this could lead to temperature inversions and substantial changes in cloud cover[3–6], but no previous modelling of the hothouse regime has resolved convective-scale turbulent air motions and cloud cover directly, thus leaving many questions about hothouse radiative heating unanswered. Here we conduct simulations that explicitly resolve convection and find that lower-tropospheric radiative heating in hothouse climates causes the hydrologic cycle to shift from a quasi-steady regime to a 'relaxation oscillator' regime, in which precipitation occurs in short and intense outbursts separated by multi-day dry spells. The transition to the oscillatory regime is accompanied by strongly enhanced local precipitation fluxes, a substantial increase in cloud cover, and a transiently positive (unstable) climate feedback parameter. Our results indicate that hothouse climates may feature a novel form of 'temporal' convective self-organization, with implications for both cloud coverage and erosion processes.

For the past few million years, Earth's climate has been characterized by fairly cool conditions, with repeated transitions between glacial and interglacial climates[7]. On longer timescales, however, the range of Earth's climate states is far wider. In the Hadean and Archaean eons[8,9], as well as in the aftermath of Neoproterozoic snowball events[10], high carbon dioxide levels may have elevated surface temperatures by tens of degrees kelvin compared to today. In the distant future, increases in solar luminosity will cause surface temperature to increase and eventually drive Earth through a runaway greenhouse transition[11]. No matter the forcing mechanism, warming of Earth's climate causes atmospheric water vapour to accumulate rapidly, strengthening the water vapour greenhouse effect by rendering more of the infrared spectrum opaque. With sufficient warming, even the most weakly absorbing spectral 'window' regions in the thermal infrared are closed off and the lower troposphere can no longer cool by emitting infrared radiation to space[12,13]. However, because water vapour also absorbs in the near-infrared spectral region[2], tropospheric absorption of incoming solar radiation persists in extremely warm climates, eventually yielding net lower-tropospheric radiative heating (LTRH). This phenomenon may also occur on the intensely irradiated daysides of tidally locked exoplanets[4], the climates of which are strongly influenced by convection near the substellar point[14–16].

Simulations of hothouse climates

We investigated hothouse climates using a convection-resolving model in which radiative and convective heating rates are constrained to be in time-mean balance (see Methods for further details). The model we employ (Das Atmosphärische Modell; DAM[17]) is fully compressible and nonhydrostatic, and is well suited to simulating very warm climates in two key respects: it takes into account the full thermodynamics of moist air, including changes in atmospheric pressure due to condensation and the effect of water on the heat capacity of air; and the radiative transfer scheme has been modified to remain accurate in very warm climates (see Methods for further details). For simulations with a time-evolving sea surface temperature (SST), the model SST is evolved according to the sum of surface enthalpy fluxes, radiative fluxes and a prescribed ocean heat sink; we also performed simulations with fixed SST. Our baseline simulations were conducted on a 72 km × 72 km square grid with doubly periodic horizontal boundary conditions. Further information about our model setup is available in the Methods.

Figure 1 shows results from a convection-resolving simulation that was initiated with an SST comparable to the warmest on Earth today (305 K, or 32 °C), but with a 10% increase in the solar constant—equivalent to Earth about 1 billion years in the future, or on an orbit about 5% closer to the Sun today. In response to this large solar forcing, the model warms rapidly and reaches a new equilibrium at a mean SST of about 330 K (57 °C) within 4 years of model time. A fundamental shift in state is evident in Fig. 1b–d, which shows time series of hourly precipitation and near-surface moist static energy during the model evolution. The early stages of the simulation are in a quasi-steady convective regime, with hourly precipitation rates exhibiting noisy fluctuations about a mean of approximately 5 mm day^{-1}. Later in the simulation, as the SST warms above about 320 K, the nature of the precipitation changes fundamentally. Rather than exhibiting noisy

[1]Department of Earth and Planetary Sciences, Harvard University, Cambridge, MA, USA. [2]School of Engineering and Applied Sciences, Harvard University, Cambridge, MA, USA.
✉e-mail: jacob.t.seeley@gmail.com

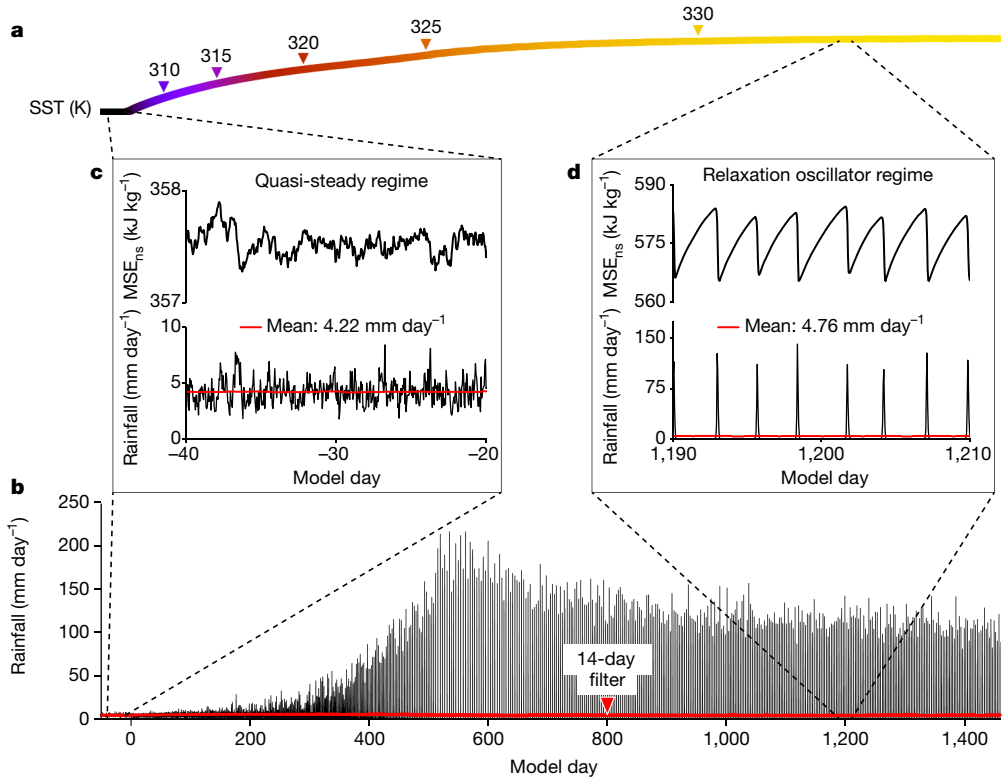

Fig. 1 | Transition to the relaxation oscillator regime due to increased insolation. The results are from a simulation initiated from an equilibrated state with a mean SST of 305 K but with a 10% increase in the solar constant, imposed on model day 0 in this figure. **a**, Fourteen-day-filtered SST with first crossings indicated for 5-K increments above 305 K. **b**, Hourly (black) and 14-day-filtered (red) precipitation. **c**, **d**, Hourly precipitation and mean near-surface ($z < 1$ km) moist static energy (MSE_{ns}) over 20-day intervals before and after the transition to the relaxation oscillator regime. Moist static energy is defined as $MSE = c_pT + Lq_v + gz$, where c_p (J kg^{-1} K^{-1}) is the heat capacity of air at constant pressure, T (K) is the temperature, L (J kg^{-1}) is the latent heat of vaporization, q_v (kg kg^{-1}) is the specific humidity, g (m s^{-2}) is the gravitational acceleration, and z (m) is the altitude.

fluctuations about the mean, precipitation occurs in large outbursts lasting a few hours, separated by regular multi-day dry spells during which there is essentially no precipitation. As in a canonical relaxation oscillator[18,19], the latter regime is characterized by repeated sequences of slow destabilization and fast stabilization (Fig. 1d); hence, we refer to this hothouse state as a 'relaxation oscillator' or 'oscillatory' regime. As our simulations receive constant diurnally averaged insolation (see Methods for further details), the emergence of periodic behaviour must be the result of radiative–convective feedbacks. Across the transition to the relaxation oscillator regime, the intensifying dry spells balance the increasingly large outbursts of precipitation such that time-mean rainfall before and after the transition changes by only about 10% (Fig. 1b–d; 14-day-filtered rainfall), as predicted by mean energetic constraints[20,21]. However, the maximum domain-mean hourly rain rates increase by an order of magnitude in the oscillatory regime.

While Fig. 1 shows that the oscillatory regime can result from solar-forced warming, the closing of the water vapour spectral windows is fundamentally tied to increased temperature and should occur regardless of the forcing mechanism. Indeed, our tests suggest that the oscillatory state is a general property of very warm and moist atmospheres simulated by convection-resolving models, being robust to forcing mechanism, microphysics scheme, domain size and resolution, and choice of convection-resolving model (Extended Data Fig. 3). To further confirm the central importance of LTRH, we conducted simulations across a range of surface temperatures with idealized time-invariant radiative heating profiles that resemble either cool-climate conditions (with radiative cooling throughout the troposphere) or hothouse conditions (with LTRH). The cool-climate radiative heating profiles produce quasi-steady convective behaviour at all temperatures (LTRH_off; Fig. 2a, d), whereas the hothouse-type radiative heating profiles produce the relaxation oscillator regime at all temperatures (LTRH_on; Fig. 2c, f). The simulations with radiation calculated interactively interpolate between these two regimes (Fig. 2b, e), suggesting that LTRH is the key characteristic of hothouse climates that drives the transition to the relaxation oscillator regime.

Physical basis of the oscillatory regime

To reveal the mechanism behind the oscillatory state, we studied high-frequency output from fixed-SST simulations at 330 K. This output shows that the oscillatory state consists of three main phases: recharge, triggering and discharge (Fig. 3). An animation of model output in the oscillatory state can be viewed in Supplementary Video 1, and a summary schematic of the phases of the oscillatory state is presented in Fig. 4a.

During an outburst of precipitation (discharge phase), the lower troposphere is flooded with negatively buoyant downdraughts of cold and dry air with low moist static energy (Fig. 3f and Supplementary Video 1). Over the course of the ensuing recharge phase, LTRH keeps the surface and the upper troposphere decoupled by increasing the mean potential temperature in the intervening 'inhibition layer' (Fig. 3e) and suppressing surface buoyancy fluxes. With the inhibition layer effectively throttling surface-based convection, surface evaporation humidifies the near-surface air without any compensating ventilation into the upper troposphere (Fig. 3a), while radiative cooling aloft cools the upper troposphere; combined, these processes lead to a large build-up of convective instability (Fig. 3f). Over the course of a few days, this build-up leaves the atmosphere primed for an intense precipitation event—a powder keg ready to explode.

The explosion of the powder keg is ultimately triggered from the top down by the influence of elevated convection. In the absence of

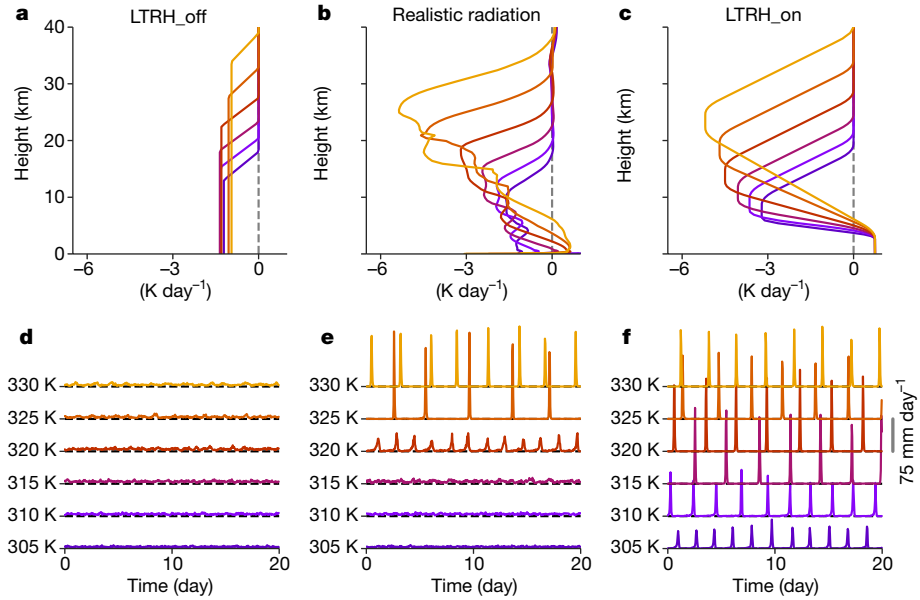

Fig. 2 | The oscillatory regime is induced by LTRH. a–**c**, Vertical profiles of radiative heating from the LTRH_off (**a**), fixedSST (**b**) and LTRH_on (**c**) simulations (see Methods for further details). The fixedSST simulations use realistic radiative transfer calculated with the model-generated vertical profiles of temperature and absorber densities, while for the other two experiments, the radiative heating profiles are prescribed to resemble either cool-climate conditions (radiative cooling throughout the troposphere; LTRH_off) or hothouse conditions (radiative heating in the lower troposphere; LTRH_on). Cool to warm colours indicate increasing SST. **d**–**f**, Twenty-day time series of domain-mean precipitation from the simulations. For visual clarity, the precipitation data are offset vertically by 75 mm day^{-1} (scale bar (grey) at right) for each 5-K increment of SST.

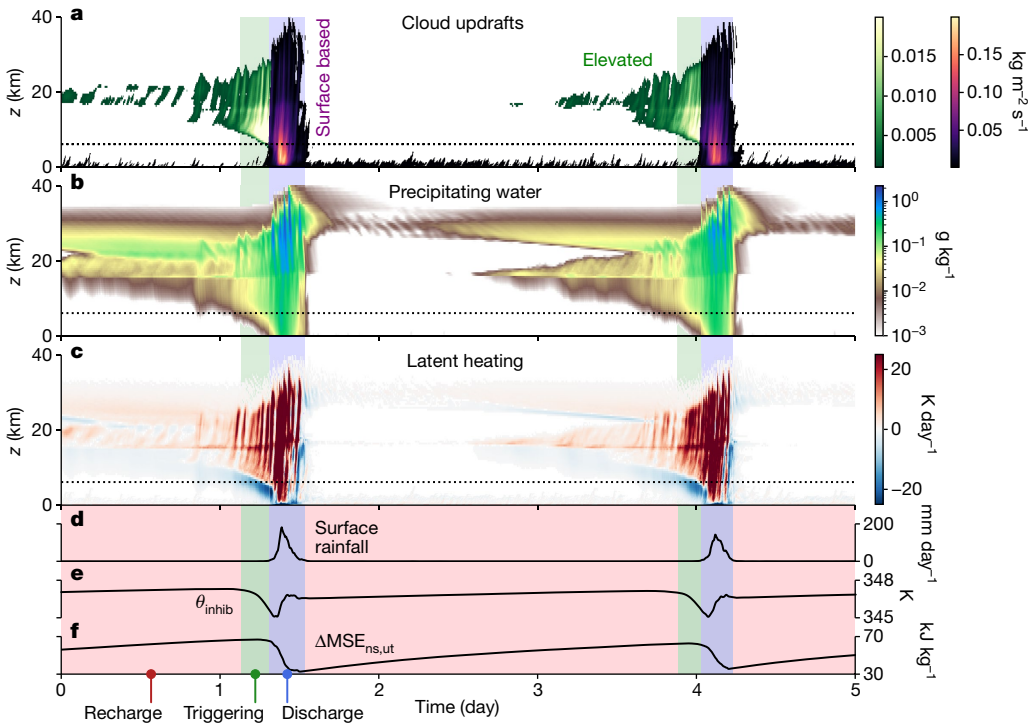

Fig. 3 | Mechanism of the oscillatory regime as revealed by high-frequency model output. a–**c**, Time-versus-height plots of cloud updraught mass flux (**a**), precipitating water mass fraction q_p (**b**), and latent heating from the fixedSST simulation at 330 K (**c**). Convective mass flux was divided into 'surface based' and 'elevated' categories using a passive tracer (see Methods for further details). **d**–**f**, Time series of domain-mean surface precipitation (**d**), θ_{inhib}, the mean potential temperature in the inhibition layer ($2{,}000 < z < 5{,}500$ m; **e**), and difference in mean moist static energy between the near-surface layer ($z < 1$ km) and the upper troposphere (ut; $25 < z < 35$ km) (**f**) from the same simulation. The discharge phases in this figure (blue shading) are identified as intervals with a surface precipitation rate above 5 mm day^{-1}. The triggering phases (green shading) begin when the hourly mean latent heating rate in the inhibition layer is more negative than −2 K day^{-1} and the surface precipitation rate is less than 1 mm day^{-1}, and end when the ensuing discharge period commences. The recharge phases occur between the end of a discharge phase and the beginning of a triggering phase. The dotted horizontal lines in **a**–**c** mark the level of zero radiative heating (that is, the transition from time-mean radiative heating to cooling).

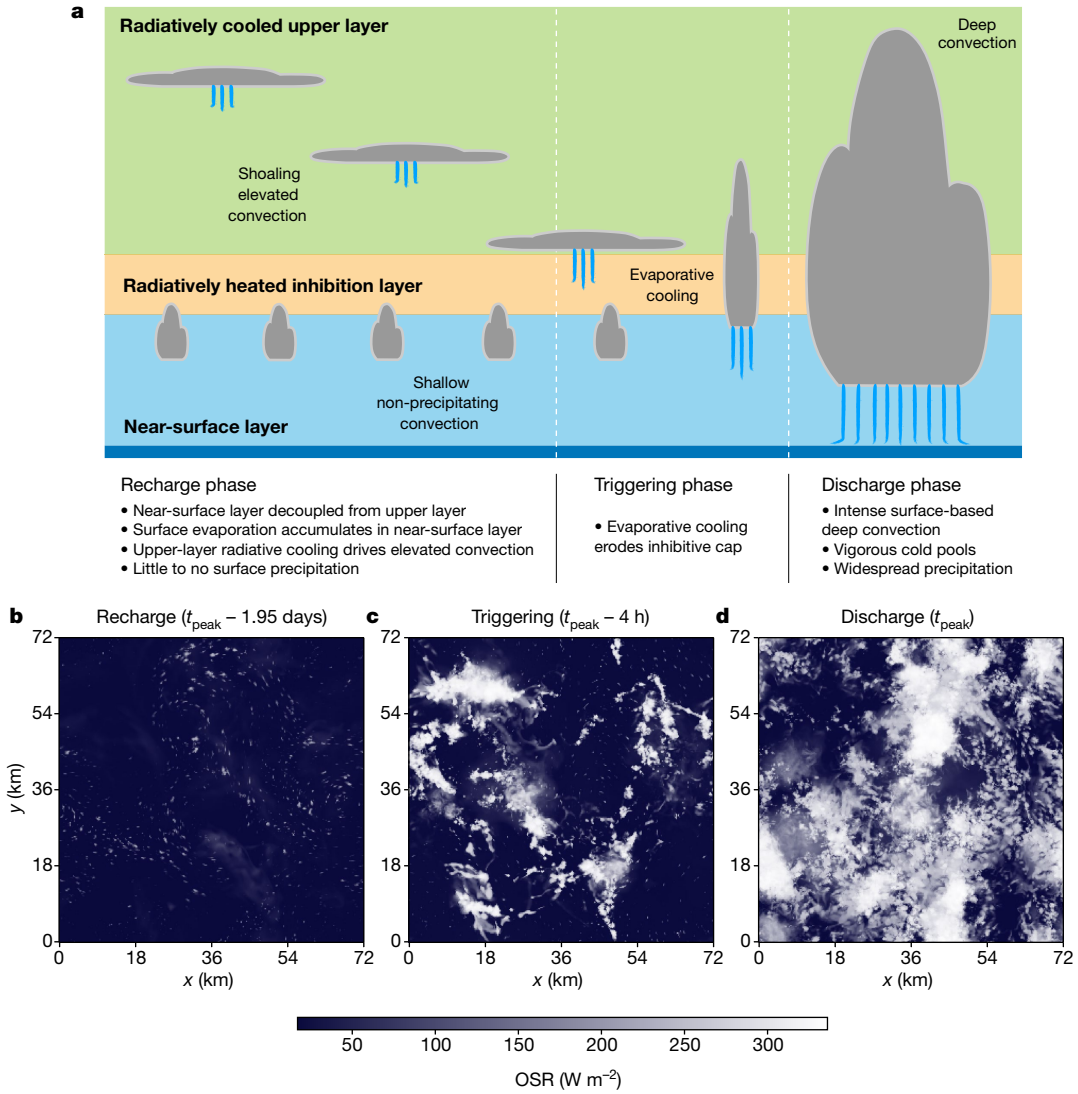

Fig. 4 | Overview of the relaxation oscillator convective regime. **a**, Schematic view of the phases of the relaxation oscillator convective regime. **b**–**d**, Snapshots of outgoing solar radiation (OSR) during the recharge (**b**), triggering (**c**), and discharge (**d**) phases, obtained 1.95 days, 4 h, and 0 h before the next hour of peak precipitation (t_{peak}), respectively. These snapshots are from the high-resolution fixed-SST simulation at a surface temperature of 330 K. High values of OSR indicate cloud cover. Neither the graphical width of the phases nor the vertical thickness of the atmospheric layers in this schematic is proportional to the amount of time or space that they occupy.

subsidence warming and drying that would keep clear air unsaturated, radiative cooling aloft during the recharge phase leads to in situ cooling, condensation and elevated convection with cloud bases above 7 km. This elevated convection produces virga (precipitation that evaporates before reaching the ground), and as the recharge phase progresses, the base of the elevated convection moves lower in altitude and the virga falls lower in the atmosphere until it begins to evaporate within the radiatively heated layer (Fig. 3a–c). The arrival of virga in the inhibition layer produces evaporative cooling rates that are approximately 20 times larger in magnitude than the antecedent radiative heating, rapidly cooling and humidifying the inhibitive cap (Fig. 3e).

The sudden weakening of the inhibition serves as a triggering mechanism that allows a small amount of surface-based convection to penetrate into the upper troposphere for the first time in several days. Once the inhibitive cap is breached, a chain reaction ensues, and the discharge phase commences: vigorous convection emanating from the near-surface layer produces strong downdraughts, which spread out along the surface as 'cold pools' (that is, gravity currents) and dynamically trigger additional surface-based deep convection[22–25]. This process proceeds for a few hours, until enough convective instability has been released such that air from the near-surface layer is no longer highly buoyant in the upper troposphere. The precipitation outburst dies out, and the cycle restarts with the recharge phase.

Comparison to parameterized convection

The convectively resolved hothouse state has both similarities and differences to prior results from models with parameterized convection. An important difference is that the time-mean temperature profile in our oscillating simulations does not resemble the three-layered structure identified in previous work[2–6], with a substantial surface-based temperature inversion capped by a deep non-condensing layer and an overlying condensing layer further aloft. Instead, our simulations have tropospheric lapse rates that fall somewhere between the dry and moist adiabats (Extended Data Fig. 4a), consistent with prior evidence that entraining moist convection sets the temperature profile in the deeply convecting tropics[26,27]. Lacking a surface-based temperature inversion, our hothouse climate simulations energetically balance

LTRH primarily by the latent cooling of rain evaporation rather than sensible heating of the surface. To further assess the importance of precipitation evaporation in the hothouse climate state, we modified the microphysics parameterization in the model to prevent evaporation of precipitating hydrometeors (rain, snow and graupel). In contrast to the corresponding case with default microphysics, LTRH in the model without hydrometeor evaporation induces a mean temperature profile closely resembling the three-layered structure from previous work with parameterized convection (Extended Data Fig. 4a). This suggests that the effects of evaporating hydrometeors on convective triggering and/or tropospheric energetics are critical to hothouse climates. In some global climate models (GCMs), evaporation of precipitation is either neglected or parameterized in a highly idealized manner[28], which may be why some previous studies concluded that surface-based inversions are a defining characteristic of hothouse atmospheres[3].

Our simulations also help clarify prior results from GCMs regarding changes in cloud cover and climate stability in hothouse states. Previous work has suggested that LTRH causes clouds to thin or disappear from the lower troposphere and thicken in a layer of elevated convection in the upper troposphere[3,6,29]. Similarly, in our model, elevated condensation and convection during the recharge phase enhance (by a factor of 3–4) the mean upper-tropospheric cloud fraction (Extended Data Fig. 4b), although shallow clouds do not disappear entirely. A further similarity between our simulations and results from GCMs is the existence of a transient climate instability (that is, a temporary sign reversal of the climate feedback parameter) during the transition to the new state induced by LTRH[3,5,6]. In our model, the instability consists of a clear-sky longwave feedback driven by enhanced upper-tropospheric RH, which is substantially amplified by the increase in upper-tropospheric cloud cover in the oscillatory state (Extended Data Fig. 5). Even for resolved convection, the net cloud radiative effect is sensitive to model details such as the horizontal resolution and microphysics scheme[30,31], so the radiative effects of clouds in the oscillatory state deserve additional study. The region of enhanced climate sensitivity associated with the transition to the hothouse state is distinct from the climate sensitivity peak found in our model at lower temperatures[32], the latter of which has been explained in terms of clear-sky feedbacks that operate in the quasi-steady convective regime[13].

Analogy to spontaneous synchronization

Spatial self-aggregation of convection, in which precipitating clouds localize in the horizontal into large and persistent clusters despite spatially uniform forcing and boundary conditions, has received considerable attention in recent years[33]. The new relaxation oscillator regime revealed by our work is an analogous state of temporal convective self-aggregation: in the absence of any time-dependent forcing, deep precipitating convection becomes spontaneously synchronized (that is, temporally localized). The oscillatory state is synchronized in the sense that subdomains separated by hundreds of kilometres exhibit boom–bust cycles of near-surface moist static energy and spikes of precipitation that are nearly in-phase (Extended Data Fig. 6). The phenomenology of this synchronized atmospheric state closely resembles that of other natural systems that exhibit spontaneous synchronization[34], such as mechanical metronomes on a wobbly platform[35] and fields of flashing fireflies[36]. In such systems, the key ingredient that allows for synchronization is a coupling that tends to align the phases of subcomponents. In the atmosphere, there are two obvious sources of coupling between spatially separated subdomains: gravity waves, which rapidly homogenize temperatures in the free troposphere[37,38]; and cold pools, which dynamically trigger additional deep convection in the neighbourhood of prior deep convection[22,23]. To investigate this analogy further, we constructed a simple two-layer model of radiative–convective equilibrium (RCE) that resembles a network of noisy pulse-coupled oscillators[34] (see Methods for further details). Just as in the convection-resolving model, this two-layer model undergoes a steady-to-oscillatory transition when the amount of convective inhibition is increased (Extended Data Fig. 7).

Discussion

The hothouse convection described here bears similarities to today's climate in the Great Plains of central USA, where elevated mixed layers transiently suppress surface-based convection until a triggering mechanism overcomes the inhibition and intense convection ensues[39–41]. Our results indicate that in hothouse climates, widespread radiatively generated convective inhibition may shift the spectrum of convective behaviour away from the quasi-equilibrium regime[42,43] and towards an 'outburst' regime more similar to that of the US Great Plains. As very warm climates have strongly reduced Equator–pole temperature gradients[3,5], tropical SSTs of 330–340 K would be accompanied by moist and temperate high latitudes that might support LTRH and the convective outburst regime over a large fraction of Earth's surface. Nonetheless, an important avenue for future work is to understand how the convective outburst regime described here interacts with large-scale overturning circulations in the tropics, as well as how this regime is expressed at higher latitudes where planetary rotation and seasonal effects play an important role in atmospheric dynamics. Convection-resolving simulations on near-global domains could address these questions, and would also shed light on the prospect of convective synchronization at scales larger than we have investigated here.

It is widely recognized that most of the geological work done by precipitation (that is, erosion, physical weathering or sediment transport) is associated with large rain events, such that a small number of intense storms play a larger role than many small ones[44]. Although our oscillating simulations have mean precipitation rates similar to their quasi-steady counterparts, local precipitation fluxes are dramatically enhanced in the oscillatory regime. For example, in our large-domain oscillating simulation with an SST of 330 K, watershed-sized areas ($\simeq$1,000 km^2) regularly experience 6-h rain accumulations of several hundred millimetres, comparable to multi-day rainfall totals along the track of landfalling tropical cyclones in the USA[45]. Such large rain accumulations do not occur at all in our quasi-steady simulations (Extended Data Fig. 8). If LTRH in very warm climates leads to similar oscillatory convective behaviour over land, the dramatically increased frequency of intense precipitation events would increase the fraction of rain that is converted to runoff, and presumably cause a substantial acceleration of rain-induced surface alteration. Such a shift in rainfall intensity could strengthen the silicate weathering feedback well beyond the upper limit inferred from energetic constraints on the mean precipitation rate[46], and in principle might even leave an isotopic signature in the geological record[47,48]. While the ~320 K SST threshold for the oscillatory transition in our model is above proxy-based estimates of peak tropical SSTs during the Phanerozoic eon[49], such temperatures could have been reached in earlier periods of Earth history, such as the high-CO_2 climates predicted in the aftermath of Neoproterozoic snowball events[10].

Finally, our work has also revealed the potentially important influence of clouds on top-of-atmosphere radiative fluxes in hothouse climates: in our oscillating simulations, elevated condensation and convection during the recharge phase enhance cloud cover, the planetary albedo and the longwave greenhouse effect. This could be particularly relevant to tidally locked planets orbiting M stars for two reasons: their daysides receive permanent instellation; and the M-star spectrum is shifted towards the near-infrared spectral region. Both of these factors would enhance shortwave absorption by water vapour[2], and might therefore make the oscillatory convective regime more likely to occur. Indeed, in simulations with an M-star insolation spectrum, we find that the transition to the oscillatory regime occurs at a lower SST than in our standard simulations (Extended Data Fig. 9). Previous

work using a global model with parameterized convection found that LTRH thinned upper-tropospheric cloud decks and led to runaway warming on tidally locked planets[4], which runs counter to the trend in high cloud amount we find in our model. These divergent model predictions highlight the importance of investigating the runaway greenhouse transition on Earth-like and tidally locked planets using global convection-resolving models in the future.

Online content

Any methods, additional references, Nature Research reporting summaries, source data, extended data, supplementary information, acknowledgements, peer review information; details of author contributions and competing interests; and statements of data and code availability are available at https://doi.org/10.1038/s41586-021-03919-z.

1. Steffen, W. et al. Trajectories of the Earth System in the Anthropocene. *Proc. Natl Acad. Sci. USA* **115**, 8252–8259 (2018).
2. Wordsworth, R. D. & Pierrehumbert, R. T. Water loss from terrestrial planets with CO_2-rich atmospheres. *Astrophys. J.* **778**, 154 (2013).
3. Wolf, E. T. & Toon, O. B. The evolution of habitable climates under the brightening Sun. *J. Geophys. Res. Atmos.* **120**, 5775–5794 (2015).
4. Kopparapu, R. K. et al. The inner edge of the habitable zone for synchronously rotating planets around low-mass stars using general circulation models. *Astrophys. J.* **819**, 84 (2016).
5. Popp, M., Schmidt, H. & Marotzke, J. Transition to a Moist Greenhouse with CO_2 and solar forcing. *Nat. Commun.* **7**, 10627 (2016).
6. Wolf, E. T., Haqq-Misra, J. & Toon, O. B. Evaluating climate sensitivity to CO_2 across Earth's history. *J. Geophys. Res. Atmos.* **123**, 11861–11874 (2018).
7. Snyder, C. W. Evolution of global temperature over the past two million years. *Nature* **538**, 226–228 (2016).
8. Sleep, N. H. The Hadean-Archaean environment. *Cold Spring Harb. Perspect. Biol.* https://doi.org/10.1101/cshperspect.a002527 (2010).
9. Charnay, B., Le Hir, G., Fluteau, F., Forget, F. & Catling, D. C. A warm or a cold early Earth? New insights from a 3-D climate-carbon model. *Earth Planet. Sci. Lett.* **474**, 97–109 (2017).
10. Pierrehumbert, R., Abbot, D., Voigt, A. & Koll, D. Climate of the Neoproterozoic. *Annu. Rev. Earth Planet. Sci.* **39**, 417–460 (2011).
11. Goldblatt, C. & Watson, A. J. The runaway greenhouse: implications for future climate change, geoengineering and planetary atmospheres. *Philos. Trans. R. Soc. A* **370**, 4197–4216 (2012).
12. Koll, D. D. B. & Cronin, T. W. Earth's outgoing longwave radiation linear due to H_2O greenhouse effect. *Proc. Natl Acad. Sci. USA* **115**, 10293–10298 (2018).
13. Seeley, J. T. & Jeevanjee, N. H_2O windows and CO_2 radiator fins: a clear-sky explanation for the peak in equilibrium climate sensitivity. *Geophys. Res. Lett.* **48**, e2020GL089609 (2021).
14. Yang, J., Cowan, N. B. & Abbot, D. S. Stabilizing cloud feedback dramatically expands the habitable zone of tidally locked planets. *Astrophys. J. Lett.* **771**, L45 (2013).
15. Sergeev, D. E. et al. Atmospheric convection plays a key role in the climate of tidally-locked terrestrial exoplanets: insights from high-resolution simulations. *Astrophys. J.* **894**, 84 (2020).
16. Lefèvre, M., Turbet, M. & Pierrehumbert, R. 3D convection-resolving model of temperate, tidally locked exoplanets. *Astrophys. J.* **913**, 101 (2021).
17. Romps, D. M. The dry-entropy budget of a moist atmosphere. *J. Atmos. Sci.* **65**, 3779–3799 (2008).
18. Wang, D. in *Wiley Encyclopedia of Electrical and Electronics Engineering* (ed. Webster, J. G.) Vol. 18, 396–405 (Wiley, 1999).
19. Ginoux, J.-M. & Letellier, C. Van der Pol and the history of relaxation oscillations: toward the emergence of a concept. *Chaos* **22**, 023120 (2012).
20. Pendergrass, A. G. & Hartmann, D. L. The atmospheric energy constraint on global-mean precipitation change. *J. Clim.* **27**, 757–768 (2014).
21. Jeevanjee, N. & Romps, D. M. Mean precipitation change from a deepening troposphere. *Proc. Natl Acad. Sci. USA* **115**, 11465–11470 (2018).
22. Torri, G., Kuang, Z. & Tian, Y. Mechanisms for convection triggering by cold pools. *Geophys. Res. Lett.* **42**, 1943–1950 (2015).
23. Jeevanjee, N. & Romps, D. M. Effective buoyancy, inertial pressure, and the mechanical generation of boundary layer mass flux by cold pools. *J. Atmos. Sci.* **72**, 3199–3213 (2015).
24. Feng, Z. et al. Mechanisms of convective cloud organization by cold pools over tropical warm ocean during the AMIE/DYNAMO field campaign. *J. Adv. Model. Earth Syst.* **7**, 357–381 (2015).
25. Torri, G. & Kuang, Z. On cold pool collisions in tropical boundary layers. *Geophys. Res. Lett.* **46**, 399–407 (2019).
26. Singh, M. S. & O'Gorman, P. A. Influence of entrainment on the thermal stratification in simulations of radiative-convective equilibrium. *Geophys. Res. Lett.* **40**, 4398–4403 (2013).
27. Seeley, J. T. & Romps, D. M. Why does tropical convective available potential energy (CAPE) increase with warming? *Geophys. Res. Lett.* **42**, 10,429–10,437 (2015).
28. Zhao, M. Uncertainty in model climate sensitivity traced to representations of cumulus precipitation microphysics. *J. Clim.* **29**, 543–560 (2016).
29. Popp, M., Schmidt, H. & Marotzke, J. Initiation of a runaway greenhouse in a cloudy column. *J. Atmos. Sci.* **72**, 452–471 (2015).
30. Wing, A. A. et al. Clouds and convective self-aggregation in a multimodel ensemble of radiative-convective equilibrium simulations. *J. Adv. Model. Earth Syst.* **12**, e2020MS002138 (2020).
31. Becker, T. & Wing, A. A. Understanding the extreme spread in climate sensitivity within the radiative-convective equilibrium model intercomparison project. *J. Adv. Model. Earth Syst.* **12**, e2020MS002165 (2020).
32. Romps, D. M. Climate sensitivity and the direct effect of carbon dioxide in a limited-area cloud-resolving model. *J. Clim.* **33**, 3413–3429 (2020).
33. Wing, A. A., Emanuel, K., Holloway, C. E. & Muller, C. Convective self-aggregation in numerical simulations: a review. *Surv. Geophys.* **38**, 1173–1197 (2017).
34. Mirollo, R. E. & Strogatz, S. H. Synchronization of pulse-coupled biological oscillators. *SIAM J. Appl. Math.* **50**, 1645–1662 (1990).
35. Pantaleone, J. Synchronization of metronomes. *Am. J. Phys.* **70**, 992–1000 (2002).
36. Buck, J. & Buck, E. Biology of synchronous flashing of fireflies. *Nature* **211**, 562–564 (1966).
37. Bretherton, C. S. & Smolarkiewicz, P. K. Gravity waves, compensating subsidence, and detrainment around cumulus clouds. *J. Atmos. Sci.* **46**, 740–759 (1989).
38. Edman, J. P. & Romps, D. M. Beyond the rigid lid: baroclinic modes in a structured atmosphere. *J. Atmos. Sci.* **74**, 3551–3566 (2017).
39. Carlson, T. N., Benjamin, S. G. & Forbes, G. S. Elevated mixed layers in the regional severe storm environment: conceptual model and case studies. *Mon. Weather Rev.* **11**, 1453–1473 (1983).
40. Schultz, D. M., Richardson, Y. P., Markowski, P. M. & Doswell, C. A. Tornadoes in the central United States and the "clash of air masses". *Bull. Am. Meteorol. Soc.* **95**, 1704–1712 (2014).
41. Agard, V. & Emanuel, K. Clausius–Clapeyron scaling of peak CAPE in continental convective storm environments. *J. Atmos. Sci.* **74**, 3043–3054 (2017).
42. Arakawa, A. & Schubert, W. H. Interaction of a cumulus cloud ensemble with the large-scale environment, part I. *J. Atmos. Sci.* **31**, 674–701 (1974).
43. Raymond, D. in *The Physics and Parameterization of Moist Atmospheric Convection* (ed. Smith, R. K.) 387–397 (Kluwer Academic Publishers, 1997).
44. Melosh, H. J. in *Planetary Surface Processes* Ch. 10, 382–433 (Cambridge Univ. Press, 2011).
45. Villarini, G., Smith, J. A., Baeck, M. L., Marchok, T. & Vecchi, G. A. Characterization of rainfall distribution and flooding associated with U.S. landfalling tropical cyclones: analyses of Hurricanes Frances, Ivan, and Jeanne (2004). *J. Geophys. Res. Atmos.* **116**, D23116 (2011).
46. Graham, R. J. & Pierrehumbert, R. Thermodynamic and energetic limits on continental silicate weathering strongly impact the climate and habitability of wet, rocky worlds. *Astrophys. J.* **896**, 115 (2020).
47. Dansgaard, W. Stable isotopes in precipitation. *Tellus* **16**, 436–468 (1964).
48. Pausata, F. S., Battisti, D. S., Nisancioglu, K. H. & Bitz, C. M. Chinese stalagmite $\delta^{18}O$ controlled by changes in the indian monsoon during a simulated heinrich event. *Nat. Geosci.* **4**, 474–480 (2011).
49. Frieling, J. et al. Extreme warmth and heat-stressed plankton in the tropics during the Paleocene-Eocene Thermal Maximum. *Sci. Adv.* **3**, e1600891 (2017).

Methods

Cloud-resolving model

To simulate nonrotating radiative-convective equilibrium (RCE), we use the cloud-resolving model DAM (ref. [17]). RCE is an idealization of planetary atmospheres in which radiative and convective heating rates achieve time-mean balance at each altitude[50].

All DAM simulations were conducted on square, doubly periodic domains with 140 vertical levels between the surface and the free-slip, rigid lid at 60 km. Our vertical grid spacing transitions from $\Delta z = 25$ m below an altitude of 650 m, to $\Delta z = 500$ m between altitudes of 5.4 and 33 km, and finally to $\Delta z = 1{,}000$ m at altitudes above 38 km. Our default horizontal resolution was $\Delta x = \Delta y = 2$ km, and our default horizontal domain size was $L_x = L_y = 72$ km. The exceptions to this are: the transient_SO and fixedSST_large simulations, which used larger domains of $L_x = 216$ km and $L_x = 512$ km, respectively; and the fixedSST_hires simulation, which used a finer horizontal resolution of $\Delta x = 250$ m (Extended Data Table 1). For all but the fixedSST_hires simulations, the model time step was $\Delta t = 20$ s, which was sub-stepped to satisfy a Courant–Friedrichs–Lewy condition; for the fixedSST_hires simulations, we used $\Delta t = 5$ s. Overall, our model configuration is similar to the RCE_small protocol from the RCEMIP project[30,50] in which DAM participated.

Surface fluxes were modelled with bulk aerodynamic formulae. Specifically, the surface latent and sensible heat fluxes (LHF and SHF) were given by

$$\mathrm{LHF}(x,y) = \rho_1(x,y) C_\mathrm{D} \sqrt{u_1(x,y)^2 + v_1(x,y)^2 + V^2}\, L_\mathrm{v} [q_\mathrm{s}^* - q_1(x,y)]; \quad (1)$$

$$\mathrm{SHF}(x,y) = \rho_1(x,y) C_\mathrm{D} \sqrt{u_1(x,y)^2 + v_1(x,y)^2 + V^2}\, c_p [\mathrm{SST} - T_1(x,y)], \quad (2)$$

where ρ_1, q_1, (u_1, v_1) and T_1 are the density, specific humidity, horizontal winds and temperature at the first model level, $C_\mathrm{D} = 1.5 \times 10^{-3}$ is a drag coefficient, $V = 5$ m s^{-1} is a background 'gustiness', L_v is the latent heat of condensation, c_p is the specific heat capacity at constant pressure of moist air, and q_s^* is the saturation-specific humidity at the SST and sea surface pressure. The surface was given a fixed, spectrally uniform albedo of 0.07.

For simulations with a time-evolving SST (CTRL, FSOL and FCO2), we used a well-mixed slab ocean with horizontally uniform temperature and heat capacity equal to that of a liquid water layer of depth 1 m. This is a standard approach[32]. We used a depth of 1 m to speed the approach to equilibrium; even though this is shallower than Earth's mixed layer, we have shown that simulations with an infinite heat capacity (fixed-SST simulations) also exhibit the oscillatory regime, which shows that using a shallow ocean does not affect our main results. At each time step, the change in the slab's internal energy was equated to the sum of an applied ocean heat sink and the net surface enthalpy and radiative fluxes into the ocean. The applied ocean heat sink is necessary because limited-area simulations of the deeply convecting tropics are in a local runaway regime[51]: the absorbed shortwave radiation exceeds the outgoing longwave radiation by about 100 W m^{-2}. In the real atmosphere, this imbalance is accommodated by oceanic and atmospheric heat export, but in a limited-area cloud-resolving model coupled to a slab ocean, the imbalance must be countered by an artificial heat sink applied to the slab ocean or else runaway warming will ensue. We obtained the magnitude of the required heat sink by diagnosing the net enthalpy flux into the ocean averaged over the final 50 days of our standard simulation with a fixed SST (fixedSST) of 305 K. This imbalance was 104.9 W m^{-2}. Our CTRL simulation (Extended Data Table 1), which was branched from the end of the fixedSST simulation at 305 K but with the slab ocean and a prescribed ocean heat sink of this magnitude, had a mean SST of 305 K over the ensuing 50 days of integration, confirming that the inclusion of this heat sink closed the column (ocean + atmosphere) heat budget. The solar- and CO_2-induced warming experiments (FSOL and FCO2) also include this same ocean heat sink.

For all simulations, domain-mean horizontal winds were nudged to zero on a timescale of 6 h to avoid the development of stratospheric jets. To minimize artificial gravity wave reflection off the model's rigid lid, a sponge layer was also included at altitudes above 40 km in which damping was applied to all three components of the wind field.

Additional details of the DAM simulations conducted for this work are summarized in Extended Data Table 1.

Radiative transfer modelling

For shortwave and longwave radiative transfer, DAM is coupled to the fully interactive Rapid Radiative Transfer Model (RRTM)[52,53]. RRTM is a correlated-*k* code that prioritizes computational efficiency and is validated for atmospheric conditions close to those of contemporary Earth. However, RRTM can produce unphysical results for the very warm atmospheres that are our focus. Extended Data Fig. 1 shows clear-sky longwave and shortwave radiative heating rates calculated by RRTM for a series of increasingly warm moist-adiabatic soundings. The unphysical discontinuities in heating rate at around 20 km altitude in the warmer soundings appear to be due to the fact that RRTM uses different lookup tables and approximations above and below a hard-coded pressure. For cooler climates, this transition pressure occurs safely in the stratosphere and there is no heating rate discontinuity, but in warmer climates the transition pressure lands in the middle of the much taller troposphere.

To obtain more realistic radiative heating rates in very warm atmospheres, we coupled DAM to a line-by-line radiation scheme known as PCM_LBL (Planetary Climate Model, Line-By-Line; ref. [54]). This code simply solves the radiative transfer equations directly as a function of wavenumber, on a fine enough spectral grid that the heating rates in our atmospheres converge. Extended Data Fig. 1 shows that the clear-sky radiative heating rates calculated by PCM_LBL closely match those of RRTM in current tropical conditions, and do not suffer from any unphysical discontinuities in heating rate in warm atmospheres. However, PCM_LBL is a clear-sky code, so to retain the effect of cloud-radiative interactions in our simulations, we took a hybrid approach: at every call to the radiation scheme (every 200 s), we swapped out the clear-sky radiative fluxes calculated by RRTM for those calculated by PCM_LBL for the horizontal-mean clear-sky column, while retaining the cloud-radiative effects calculated by RRTM. Using the horizontal-mean clear-sky column neglects variations in radiative heating rates due to horizontal variations in water vapour. However, sensitivity tests (not shown) indicated that this had a negligible effect on our simulation results, with differences in time-mean cloud-radiative effect of order 1 W m^{-2}. Extended Data Fig. 2 shows that this approach captures cloud-radiative effects closely. These effects are the dominant source of variability in top-of-atmosphere fluxes and atmospheric heating rates in our simulations. We also note that our approach to radiation is justified by the LTRH_on experiment suite (Extended Data Table 1), which shows that the transition to the oscillatory convective regime due to LTRH does not depend on the details of cloud-radiative interactions. We validate and fully describe our radiative transfer modelling with PCM_LBL below.

Our longwave calculations with PCM_LBL covered the wavenumber range of 0–4,000 cm^{-1}, while our shortwave calculations covered 0–50,000 cm^{-1}. The spectral resolution for both channels was 0.1 cm^{-1}. While this spectral resolution does not resolve the cores of lines at very low (upper-stratospheric) pressures, sensitivity tests showed that further increases in resolution yielded negligible changes to the radiative fluxes and heating rates in the troposphere, which is our focus. Similar convergence was also found in previous work[54,55]. At each wavenumber, the monochromatic radiative transfer equation was solved using an approach described in previous work[56], which

uses the layer optical depth weighting scheme[57] to ensure accurate model behaviour in strongly absorbing portions of the spectrum. To compute radiative fluxes, we used the two-stream approximation with first-moment Gaussian quadrature[57].

PCM_LBL uses lookup tables of absorption coefficients on a pressure–temperature grid that covers the range of atmospheric conditions encountered in the model evolution, and interpolates to the current horizontal-mean atmospheric state at each vertical model level. Our pressure–temperature grid had a total of 20 pressure levels, with 10 levels spaced linearly in pressure between 110,000 Pa and 10,000 Pa, and 10 levels spaced logarithmically between 10,000 Pa and 0.1 Pa. On each pressure level, absorption coefficients were evaluated at a set of 20 temperatures (spaced 10 K apart) that bracket the conditions encountered in the model evolution. To generate the absorption-coefficient lookup tables for H_2O and CO_2 from the HITRAN2016 database[58], we used the Reference Forward Model, a contemporary line-by-line model[59]. Both PCM_LBL and RRTM use MT-CKD to calculate the water vapour continuum[60].

For shortwave radiation, we modelled gaseous absorption alone, which is appropriate for clear skies at wavelengths where Rayleigh scattering is not important. In reality, Rayleigh scattering in clear skies enhances the planetary albedo, but this process is important at substantially shorter wavelengths than the near-infrared wavelengths absorbed by H_2O. Therefore, the inclusion of Rayleigh scattering would introduce a small offset in the relationship between insolation and equilibrated surface temperature in our model, which would simply be absorbed into the oceanic heat sink. Our shortwave radiation setup differs between our M-star simulations (MSTAR) and our Earth-like experiment configurations (all other simulations with interactive radiation). For our Earth-like configurations, we used top-of-atmosphere downwelling spectral solar flux data[61] normalized to our specified values of the solar constant. For the MSTAR experiment, we used spectral instellation data from the M star AD Leonis B (ref. [62]). We did not include a diurnal cycle of insolation; for our Earth-like configurations, the cosine of the solar zenith angle was set to its insolation-weighted average during the diurnal cycle at the Equator on 1 January, yielding a zenith angle of 43.75°. With a contemporary solar constant of 1,366 W m^{-2}, this yields a downwelling shortwave flux at top-of-atmosphere of 413.13 W m^{-2}. This shortwave insolation was used for all Earth-like simulations with interactive radiation except for the FSOL simulation, which used a solar constant larger by 10%. For our MSTAR experiment, we set the cosine of the solar zenith angle to its instellation-weighted (dayside) mean, yielding a zenith angle of 48.19°, and used a stellar constant of 800 W m^{-2}.

Microphysics parameterizations

The default microphysics scheme in DAM is known as the Lin–Lord–Krueger (LLK) parameterization[63–65]. The LLK parameterization is a bulk scheme with six water classes (vapour, cloud liquid, cloud ice, rain, snow and graupel). Almost all of our DAM simulations were conducted with this microphysics scheme; however, to test the robustness of our main results to microphysics, we also conducted fixed-SST simulations at 305 K and 330 K (the fixedSST_sm suite; Extended Data Table 1) using a highly simplified microphysics scheme that has been described in previous work[66,67]; we also describe this simplified scheme below. Additionally, the prevap0 simulations used the LLK microphysics parameterization, but with all evaporation of precipitating hydrometeors (rain, snow and graupel) set to zero.

In the simplified microphysics scheme, there is no ice phase (that is, water is modelled as a two-phase substance, with latent heat associated with phase change between vapour and liquid alone). Accordingly, only three bulk classes of water substance are modelled: vapour, non-precipitating cloud liquid, and rain, with associated mass fractions q_v, q_c and q_r, respectively. Microphysical transformations between vapour and cloud condensate are handled by a saturation adjustment routine, which prevents relative humidity from exceeding 100% (that is, abundant cloud condensation nuclei are assumed to be present) and evaporates cloud condensate in subsaturated air. Conversion of non-precipitating cloud condensate to rain is modelled as autoconversion according to

$$a = -q_c/\tau_a, \tag{3}$$

where a (s^{-1}) is the sink of cloud condensate from autoconversion and τ_a (s) is an autoconversion timescale. We use τ_a = 25 min, which was found in prior work to produce a similar mean cloud fraction profile to that of the LLK microphysics scheme[67]. We did not set an autoconversion threshold for q_c. Furthermore, rain is given a fixed freefall speed of 8 m s^{-1} in this simplified microphysics scheme. When rain falls through subsaturated air, it is allowed to evaporate according to

$$e = \left(q_v^* - q_v\right)/\tau_r, \tag{4}$$

where e (s^{-1}) is the rate of rain evaporation, q_v^* is the saturation-specific humidity, and τ_r (s) is a rain-evaporation timescale. We set τ_r = 50 h, which was found in prior work to produce a tropospheric relative humidity profile similar to that of the LLK scheme[67].

Near-surface tracer

In the oscillatory state, convective mass flux can be divided into two categories: updraughts that emanate from the near-surface layer (z < 1 km); and updraughts that originate from higher in the troposphere. To discriminate between these two categories, we employed a passive tracer that measures what fraction of dry air in an updraught was recently advected from below a certain height (here, 1 km)[68]. We denote this tracer's mixing ratio as χ_{ns}. At every model time step, χ_{ns} was set to 1 at altitudes below 1 km, and set to zero above that height except in the 'vicinity' of cloudy updraughts. We define cloudy updraughts as grid cells that have vertical velocity $w \geq 0.5$ m s^{-1} and non-precipitating cloud condensate $q_n \geq 10^{-2}$ g kg^{-1}, and their 'vicinity' as a cube of side length 7 grid cells centred on the updraught[68]. Cloudy-updraught grid cells in which this tracer has a value of 0 contain no air that originated in the near-surface layer, so we assigned mass flux with a mean value of $\chi_{ns} = 0$ during our 5-min sampling interval to the 'elevated' category, and assigned the remainder to the 'surface-based' category. This is an overly stringent definition of elevated convection, as any amount of surface-based convection that occurs at a certain altitude within the 5-min sampling interval will knock other (potentially elevated) updraughts out of the 'elevated' category. Nevertheless, we still identify a large amount of elevated convection in Fig. 3a.

Simulations with other cloud-resolving models

In addition to our simulations with DAM, we also conducted simulations with two other cloud-resolving models: the System for Atmospheric Modeling (SAM)[69] and Cloud Model 1 (ref. [70]). With each model, we conducted fixed-SST simulations at 305 K and 325 K, initialized with soundings from the corresponding fixedSST DAM simulation.

For our SAM simulations, we used a domain of horizontal dimension 144 km with 2-km resolution. We used the same vertical grid as used for our DAM simulations, but extended to 64 km (for a total of 144 levels in the vertical) to satisfy parallelization requirements in SAM. We used a time step of 10 s. The radiation scheme was RRTM, and the microphysics scheme was SAM's 1-moment scheme. We ran each simulation for 100 days.

For our Cloud Model 1 simulations, we used a domain of horizontal dimension 72 km with 2 km resolution, and 100 vertical levels with a stretched grid (50-m resolution at altitudes below 650 m, and 500-m resolution at altitudes above 5,600 m). We used a time step of 20 s. The radiation scheme was RRTMG, and we used the Morrison

double-moment microphysics scheme[71]. We ran each simulation for 150 days.

Stochastic two-layer model

To explore the analogy between the oscillatory convective regime and the phenomenon of spontaneous synchronization[34], we constructed a simple two-layer model of RCE that resembles a network of noisy pulse-coupled oscillators. In this model, the two layers represent the near-surface layer and the upper troposphere. Each layer has a thermodynamic state variable T whose time evolution is governed by a combination of surface fluxes and convection (in the case of the lower layer) or radiation and convection (in the case of the upper layer). The upper layer is assumed to be well mixed (with a single T), whereas the lower layer is divided into $N = nx \times ny$ cells arranged in a two-dimensional, doubly periodic lattice, each with its own T. Each lower-layer cell is coupled to the surface by a relaxation to a surface thermodynamic state of $T_s = 0$. (The choice of T_s is arbitrary as it simply adds an offset to the temperatures of the other layers.) The two layers are coupled by convection, which we model as a stochastically triggered relaxation process that we describe in more detail below.

The governing equation for the upper-layer temperature T_u is:

$$\frac{\mathrm{d}T_u}{\mathrm{d}t} = Q + \frac{1}{N}\sum_{i,j} M_{ij}, \tag{5}$$

where Q (K day^{-1}) is the radiative heating rate in the upper troposphere (negative values indicate cooling) and M_{ij} (K day^{-1}) is the deep-convective heating rate from boundary layer cell (i, j). The governing equation for the lower layer cell temperatures T_{ij} is

$$\frac{\mathrm{d}T_{ij}}{\mathrm{d}t} = -T_{ij}/\tau_s - M_{ij}, \tag{6}$$

where τ_s is the surface-flux timescale. Note that, owing to our choice of $T_s = 0$, T_{ij} is negative (that is, the surface-flux term acts as a relaxation to the surface temperature of 0).

We model convective triggering and heating as stochastic processes. The generation of a convective event proceeds in three steps: testing whether an event is triggered; determining the magnitude of the event; and determining whether the event can overcome an externally specified convective inhibition parameter. For the first step, convective triggering in each grid cell is assumed to behave as a Poisson process, which is a generic representation of events that are rare and independent but that occur at an expected rate. Accordingly, the probability of convective triggering in a small time step Δt is given by $\exp(-\lambda\Delta t)$, where λ (day^{-1}) is the expected rate of convective triggering. If convection is triggered, the second step determines the size of the event by drawing an inverse timescale α_{ij} (day^{-1}) from an exponential distribution:

$$P(\alpha_{ij}) = \frac{1}{\beta_{ij}}\exp\left(-\alpha_{ij}/\beta_{ij}\right), \tag{7}$$

for scale parameter β_{ij}. Hence, larger inverse timescales, which correspond to larger convective mass fluxes/heating rates, are less common than smaller events. To represent the fact that downdraughts from neighbouring convection generate larger convective plumes with lower bulk entrainment rates and larger heating rates[24], we made the scale parameter β_{ij} linearly dependent on the convective heating rate in nearby grid cells:

$$\beta_{ij} = \beta_0\left(1 + \frac{M_{\mathrm{neighbours}}}{M_0}\right), \tag{8}$$

where $M_{\mathrm{neighbours}}$ is the convective heating rate summed over the 'neighbourhood' of the lower-layer cell, which we specify below. The parameter M_0 (K day^{-1}), as well as the chosen size of the neighbourhood of each lower-layer cell, together set the sensitivity of β_{ij} to neighbouring convection.

Finally, once the size of the triggered event is determined, α_{ij} is compared to the inhibition parameter I (day^{-1}). I functions as a cutoff scale: the triggered event occurs only if $\alpha_{ij} > I$. In the case of a triggered event at time t^*_{ij} that overcomes the inhibition, the convective heating rate in cell (i, j) is set as

$$M_{ij}(t) = \begin{cases} \max\left[\alpha_{ij}\left(T_{ij} - T_u\right), 0\right], & \text{for } t^*_{ij} \le t < t^*_{ij} + \tau_c \\ 0, & \text{otherwise,} \end{cases} \tag{9}$$

where τ_c is the duration of convective events. We do not allow additional convective events to trigger in a grid cell when there is an ongoing event in that grid cell. While heuristic, this model captures some of the basic features of the convective feedbacks that occur in the full RCE simulations.

The two-layer model equations are integrated numerically with a simple forward-difference Euler method. We used parameter values $Q = -1$ K day^{-1}, $\tau_s = 1$ day, $\tau_c = 1$ h, $\lambda = 12$ day^{-1}, $\beta_0 = 1$ day^{-1} and $M_0 = 1$ K day^{-1}. We defined the neighbourhood of each grid cell as a square of side length 9 grid cells centred on cell (i, j), and we used a grid of size $nx = ny = 50$ and a time step of 10 min. We checked model convergence by halving the time step twice (to 5 and 2.5 min) and found very similar results in both cases.

For Extended Data Fig. 7, we first integrated the model for 15 days with a low value of inhibition $I = 1$ day^{-1}, then integrated the model for two days while linearly increasing I to 6 day^{-1} (representing the build-up of inhibition after radiative heating is switched on in the transient_SO simulation), and finally integrated the model for another 15 days with I held fixed at the larger value.

Data availability

Input data files and cloud-resolving model output associated with this work are available in a Zenodo repository at https://doi.org/10.5281/zenodo.5117529.

Code availability

Source code for the stochastic two-layer model, processing cloud-resolving model output, and generating figures is available in a Zenodo repository at https://doi.org/10.5281/zenodo.5117529.

50. Wing, A. A. et al. Radiative-Convective Equilibrium Model Intercomparison Project. *Geosci. Model Dev.* **11**, 793–813 (2018).
51. Romps, D. M. Response of tropical precipitation to global warming. *J. Atmos. Sci.* **68**, 123–138 (2011).
52. Clough, S. A. et al. Atmospheric radiative transfer modeling: a summary of the AER codes. *J. Quant. Spectrosc. Radiat. Transf.* **91**, 233–244 (2005).
53. Iacono, M. J. et al. Radiative forcing by long-lived greenhouse gases: calculations with the AER radiative transfer models. *J. Geophys. Res. Atmos.* **113**, 2–9 (2008).
54. Wordsworth, R. et al. Transient reducing greenhouse warming on early Mars. *Geophys. Res. Lett.* **44**, 665–671 (2017).
55. Ding, F. & Wordsworth, R. D. A new line-by-line general circulation model for simulations of diverse planetary atmospheres: initial validation and application to the exoplanet GJ 1132B. *Astrophys. J.* **878**, 117 (2019).
56. Schaefer, L., Wordsworth, R. D., Berta-Thompson, Z. & Sasselov, D. Predictions of the atmospheric composition of GJ 1132b. *Astrophys. J.* **829**, 63 (2016).
57. Clough, S. A., Iacono, M. J. & Moncet, J.-L. Line-by-line calculations of atmospheric fluxes and cooling rates: application to water vapor. *J. Geophys. Res.* **97**, 15761 (1992).
58. Gordon, I. E. et al. The HITRAN2016 molecular spectroscopic database. *J. Quant. Spectrosc. Radiat. Transf.* **203**, 3–69 (2017).
59. Dudhia, A. The Reference Forward Model (RFM). *J. Quant. Spectrosc. Radiat. Transf.* **186**, 243–253 (2017).
60. Mlawer, E. J. et al. Development and recent evaluation of the MT_CKD model of continuum absorption. *Philos. Trans. R. Soc. A* **370**, 2520–2556 (2012).
61. Claire, M. W. et al. The evolution of solar flux from 0.1 nm to 160 μm: quantitative estimates for planetary studies. *Astrophys. J.* **757**, 95 (2012).
62. Segura, A. et al. Biosignatures from Earth-like planets around M dwarfs. *Astrobiology* **5**, 706–725 (2005).

63. Krueger, S. K., Fu, Q., Liou, K. N. & Chin, H.-N. S. Improvements of an ice-phase mcrophysics parameterization for use in numerical simulations of tropical convection. *J. Appl. Meteorol.* **34**, 281–286 (1995).
64. Lin, Y.-L., Farley, R. D. & Orville, H. D. Bulk parameterization of the snow field in a cloud model. *J. Clim. Appl. Meteorol.* **22**, 1065–1092 (1983).
65. Lord, S. J., Willoughby, H. E. & Piotrowicz, J. M. Role of a parameterized ice-phase microphysics in an axisymmetric, nonhydrostatic tropical cyclone model. *J. Atmos. Sci.* **41**, 2836–2848 (1984).
66. Seeley, J. T., Jeevanjee, N. & Romps, D. M. FAT or FiTT: are anvil clouds or the tropopause temperature-invariant? *Geophys. Res. Lett.* **46**, 1842–1850 (2019).
67. Seeley, J. T., Lutsko, N. J. & Keith, D. W. Designing a radiative antidote to CO_2. *Geophys. Res. Lett.* **48**, e2020GL090876 (2021).
68. Romps, D. M. & Kuang, Z. Nature versus nurture in shallow convection. *J. Atmos. Sci.* **67**, 1655–1666 (2010).
69. Khairoutdinov, M. F. & Randall, D. A. Cloud resolving modeling of the ARM summer 1997 IOP: model formulation, results, uncertainties, and sensitivities. *J. Atmos. Sci.* **60**, 607–625 (2003).
70. Bryan, G. & Fritsch, J. A benchmark simulation for moist nonhydrostatic numerical models. *Mon. Weather Rev.* **130**, 2917–2928 (2002).
71. Morrison, H., Curry, J. A. & Khvorostyanov, V. I. A new double-moment microphysics parameterization for application in cloud and climate models. Part I: description. *J. Atmos. Sci.***62**, 1665–1677 (2005).
72. Cess, R. D. et al. Intercomparison and interpretation of climate feedback processes in 19 atmospheric general circulation models. *J. Geophys. Res. Atmos.* **95**, 16601–16615 (1990).

Acknowledgements We are grateful to the authors of the cloud-resolving models used in this work: D. Romps, M. Khairoutdinov and G. Bryan. We also thank A. Dudhia for sharing with us the Reference Forward Model. We thank X. Wei for conducting exploratory simulations with SAM. J.T.S. thanks N. Jeevanjee, A. Match, N. Tarshish and Z. Kuang for discussions.

Author contributions J.T.S. and R.D.W. designed the research. J.T.S. performed the simulations, analysed the results and prepared the figures. The manuscript was written jointly by J.T.S. and R.D.W.

Competing interests The authors declare no competing interests.

Additional information

Supplementary information The online version contains supplementary material available at https://doi.org/10.1038/s41586-021-03919-z.

Correspondence and requests for materials should be addressed to Jacob T. Seeley.

Peer review information *Nature* thanks the anonymous reviewers for their contribution to the peer review of this work.

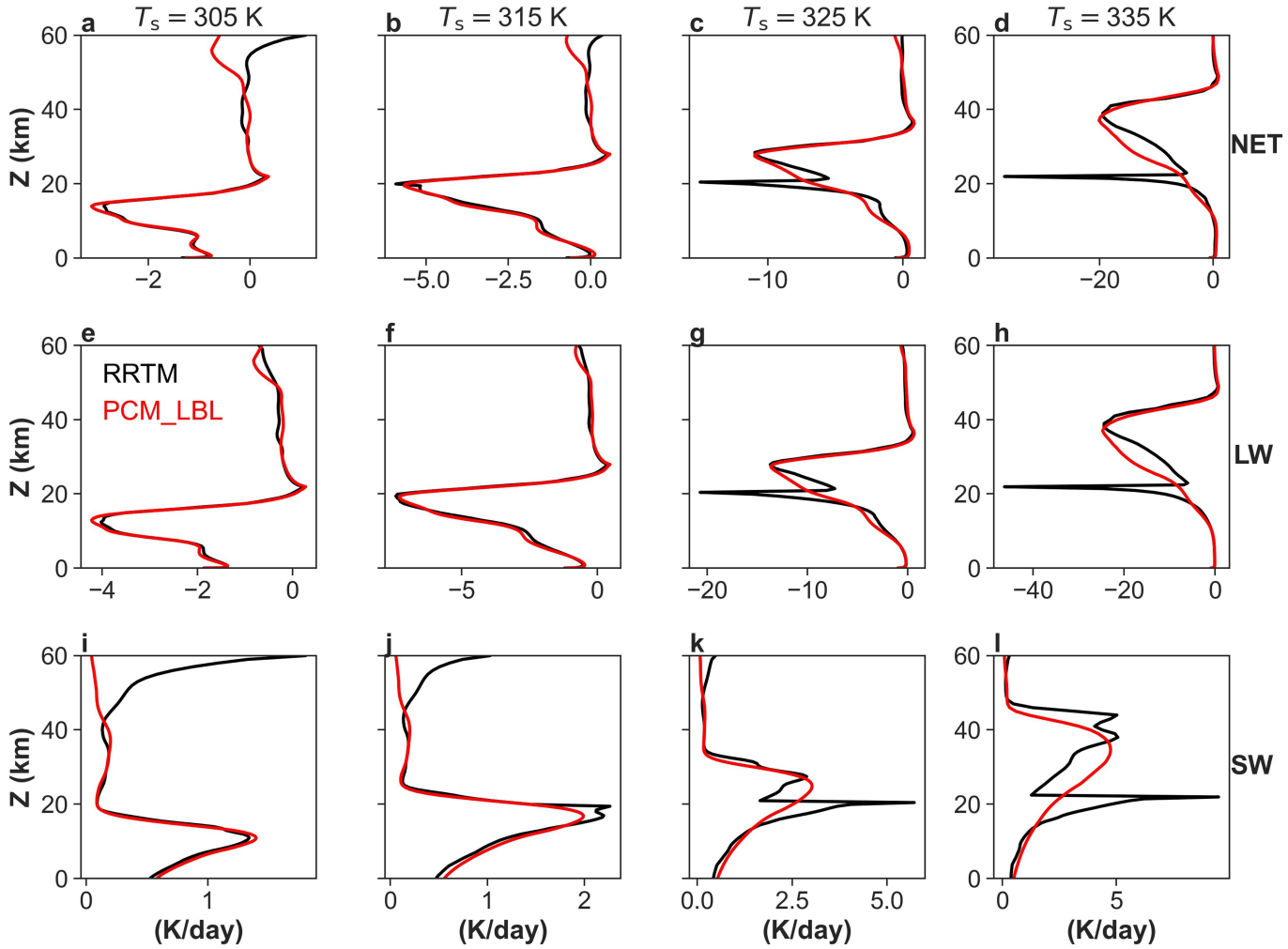

Extended Data Fig. 1 | Errors in clear-sky RRTM radiative heating rates are corrected by using line-by-line radiative transfer. Comparison of net (LW+SW; panels **a**–**d**), longwave (LW; panels **e**–**h**), and shortwave (SW; panels **i**–**l**) radiative heating rates as computed by RRTM (black) and PCM_LBL (red). The heating rates are computed for moist-adiabatic temperature-pressure profiles with surface temperatures ranging from 305 K to 335 K in 10-K increments (columns, left to right). All columns have a surface pressure of 101325 Pa, 75% tropospheric relative humidity, 400 ppm CO_2, and an isothermal stratosphere at 160 K. Note that the discontinuous heating rates calculated by RRTM for the warmer atmospheres (around 20 km altitude) do not appear in the PCM_LBL results.

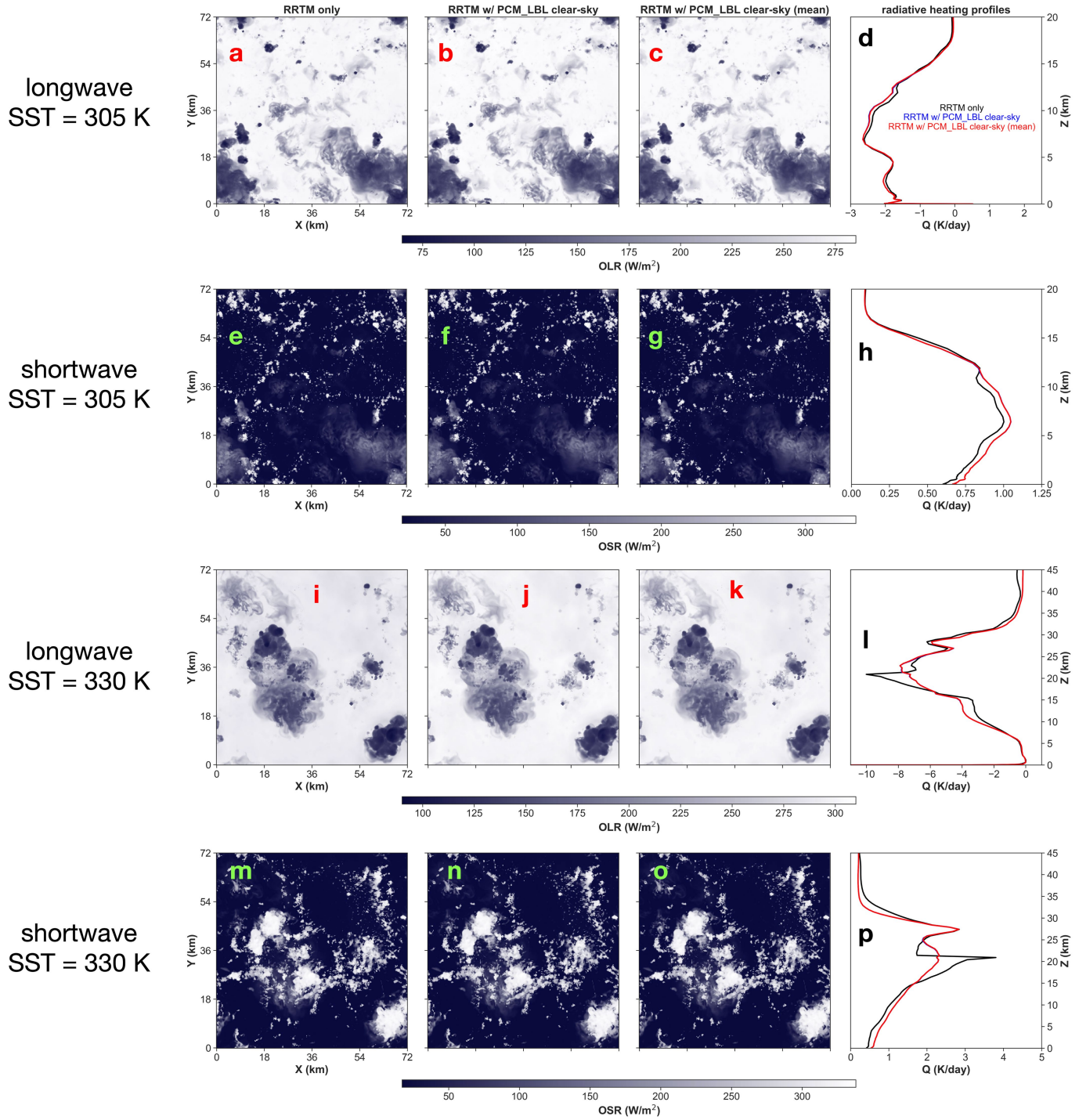

Extended Data Fig. 2 | Top-of-atmosphere radiative fluxes and heating rates from DAM snapshots. (**a**–**c**) Outgoing longwave radiation (OLR) from a snapshot from the fixedSST_hires DAM simulation with a surface temperature of 305 K, computed by three different combinations of radiative transfer codes and approximations. Panel (**a**) is from RRTM alone, panel (**b**) shows the result of swapping out the clear-sky radiative fluxes from RRTM with those calculated by PCM_LBL, and panel (**c**) shows the result of swapping out each column's clear-sky radiative fluxes for those calculated by PCM_LBL for the horizontal-mean column, which is the approach taken for the simulations associated with this work. Panel (**d**) shows the horizontal-mean longwave radiative heating rates for this snapshot. (**e**–**h**) As in (**a**–**d**), but for absorbed shortwave radiation (ASR). (**i**–**p**) As in (**a**–**h**), but for a snapshot from the simulation with a surface temperature of 330 K.

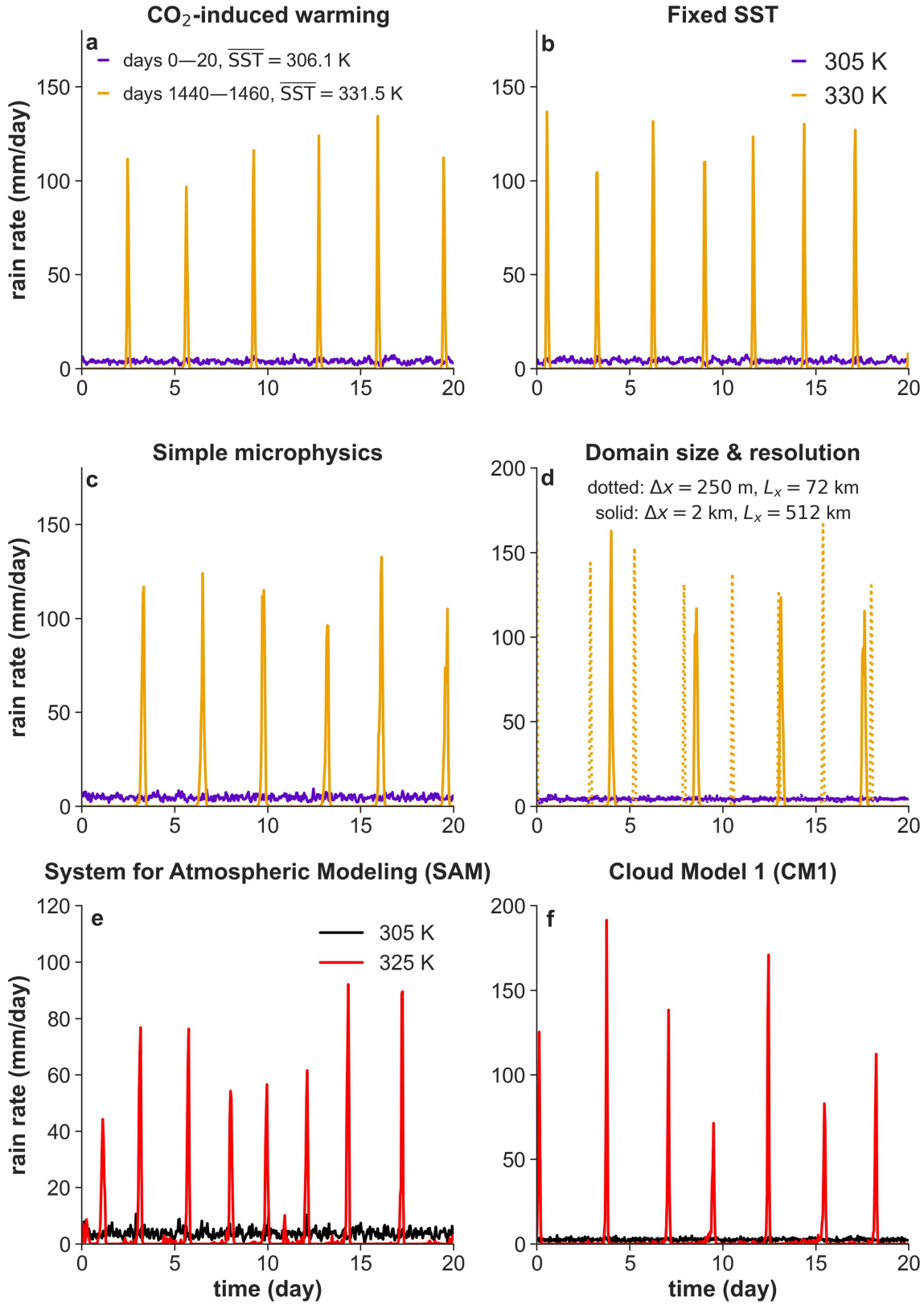

Extended Data Fig. 3 | Tests of the robustness of the oscillatory transition. Domain-mean precipitation from two periods of (**a**) the FCO2 simulation with mean SSTs of 306.1 K and 331.5 K; (**b**) the fixedSST suite at 305 K and 330 K; (**c**) the fixedSST_sm suite, which use the simplified microphysics parameterization described in the Methods; (**d**) fixed-SST simulations with finer horizontal resolution (Δx = 250 m; fixedSST_hires) or on a larger domain (L_x = 512 km; fixedSST_large). (**e**) The same quantity from simulations conducted with the System for Atmospheric Modeling (SAM)[69] at fixed SSTs of 305 and 325 K. (**f**) As in (**e**), but for the Cloud Model 1 (CM1)[70].

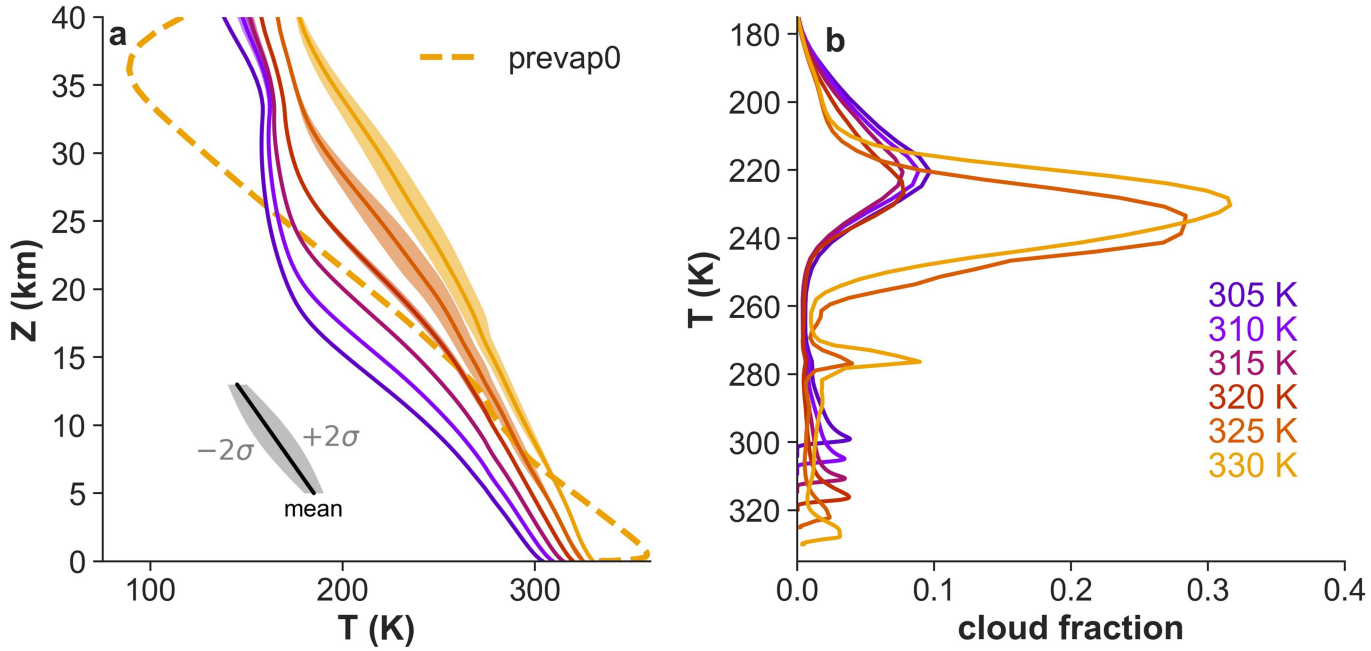

Extended Data Fig. 4 | Mean profiles of temperature and cloud fraction. From the fixedSST simulations, profiles of (**a**) mean temperature and (**b**) mean cloud fraction (fraction of grid cells with non-precipitating cloud condensate mass fraction greater than 10^{-5} kg/kg). In (**a**), the variability is indicated by the shading, which shows ±2 standard deviations of hourly-mean temperatures at each altitude. In (**a**), the dashed line shows the mean temperature profile from the simulation without evaporation of precipitating hydrometeors (prevap0) at 330 K.

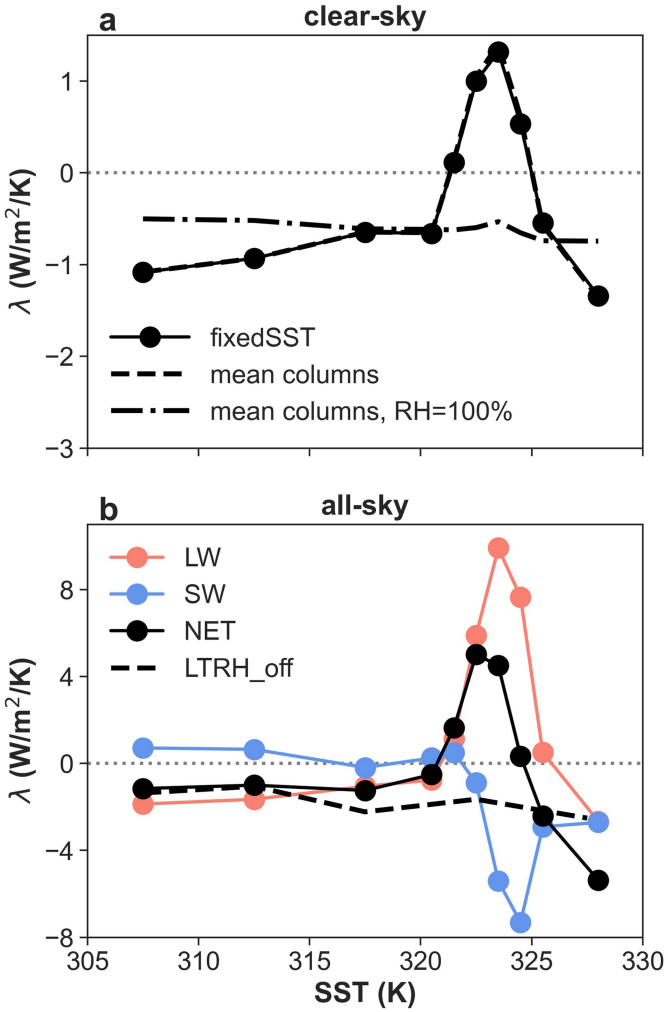

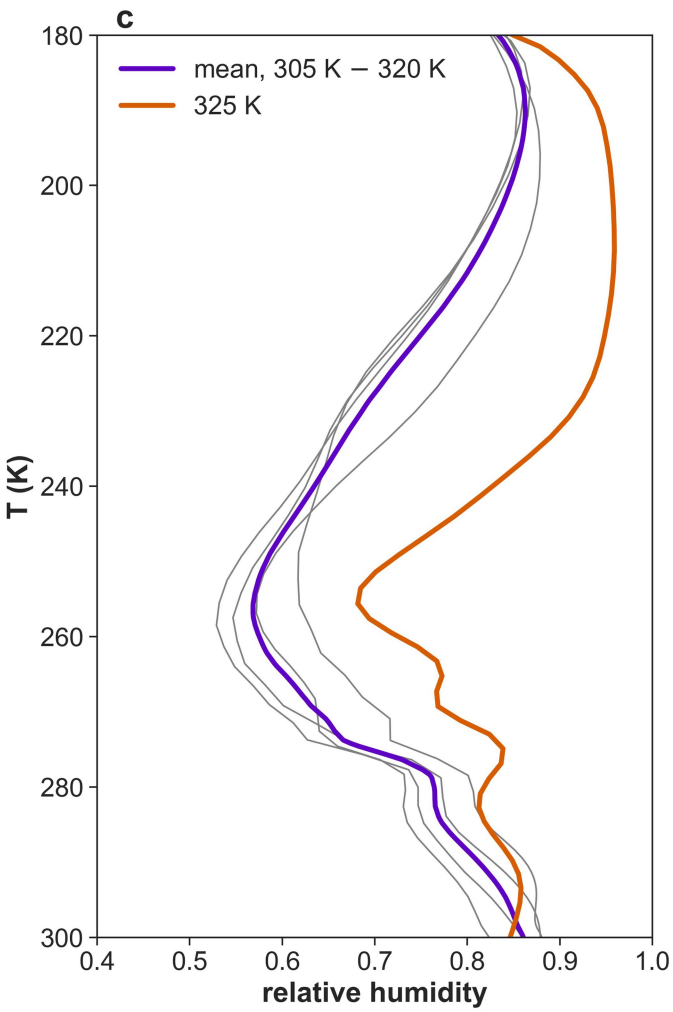

Extended Data Fig. 5 | Sign reversal of the climate feedback parameter indicates transient climate instability. The feedback parameter λ is defined here as minus the change in net radiative flux at the top-of-atmosphere (TOA) per degree of surface warming (positive downward, so that a negative feedback indicates more radiation escaping to space with warming and hence climate stability, and a positive feedback indicates climate instability; this is often called the "Cess sensitivity"[72]). We calculated feedbacks using finite differences on a staggered surface temperature grid that interpolates between the surface temperatures of the fixedSST experiment. (**a**) The solid line shows clear-sky feedbacks calculated for TOA fluxes averaged over the final 100 days of the fixedSST simulations, while the dashed and dot-dashed lines show the feedbacks calculated using the time-mean columns from those simulations with actual or fixed 100% relative humidity profiles, respectively. (**b**) As in (a), but for the all-sky feedbacks from fixedSST experiments broken down into longwave and shortwave components. The dashed line shows the net all-sky feedback from the final 50 days of the LTRH_off experiment, which does not undergo a steady-to-oscillatory transition and remains stable at all temperatures. (**c**) Time-mean profiles of relative humidity (RH) in the fixedSST experiments, using temperature within the atmosphere as a vertical coordinate to emphasize the increases in upper-tropospheric relative humidity that occur during the oscillatory transition between 320 and 325 and K. Since the clear-sky climate instability is eliminated by using a fixed relative humidity of 100% (panel a), we attribute the clear-sky climate instability to the increase in upper-tropospheric RH, which lowers spectral emission temperatures and hence OLR.

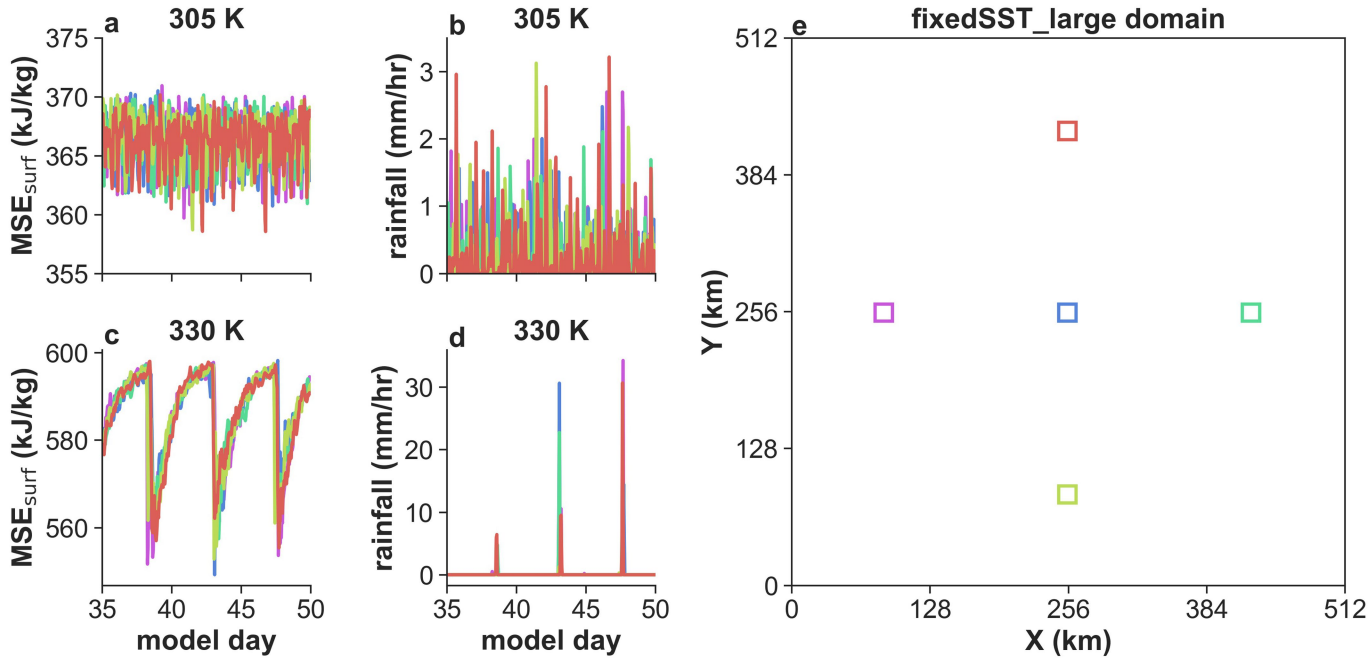

Extended Data Fig. 6 | Spatially-separated subdomains exhibit in-phase pulses of convection. Timeseries of (**a**,**c**) moist static energy in the lowest model level (z = 12.5 m; MSE$_{surf}$), and (**b**,**d**) precipitation rate, averaged over five different subdomains of the fixedSST_large simulations at 305 K (top row) and 330 K (bottom row). The subdomains (color-coded in panel e) each have an area of 256 km^2 and are located an average of 215 km apart from each other.

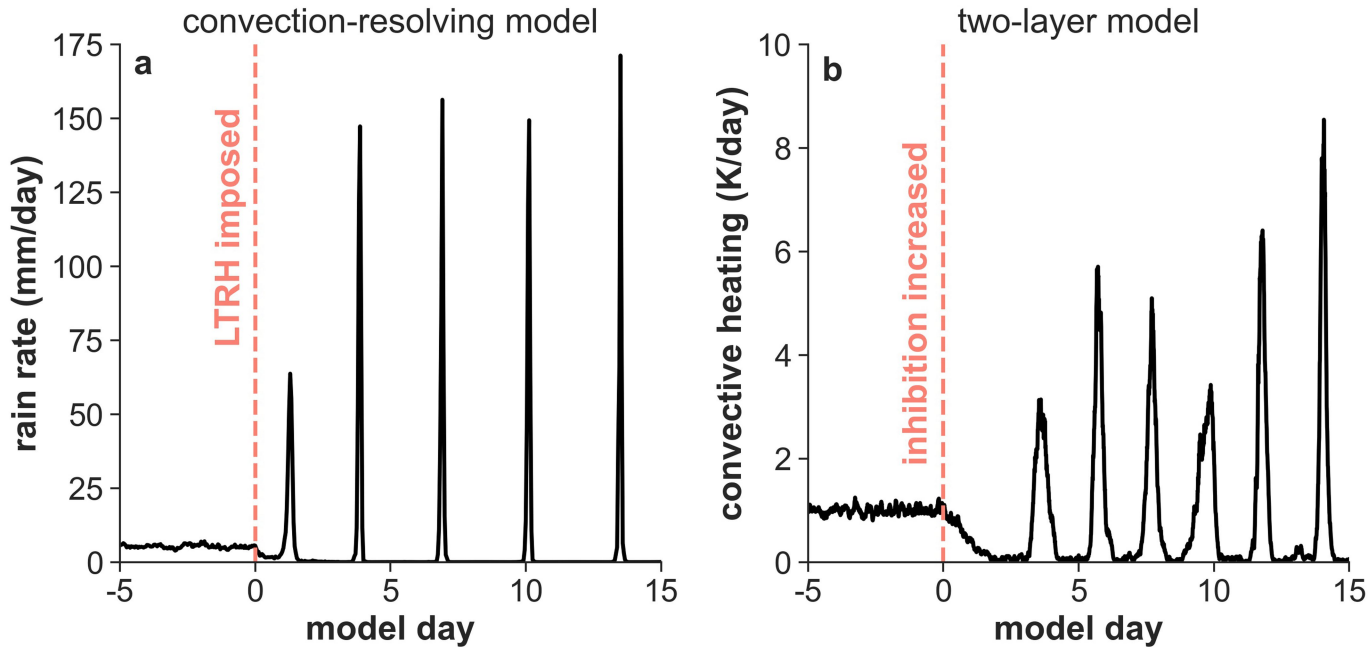

Extended Data Fig. 7 | The steady-to-oscillatory transition in the convection-resolving model and the stochastic two-layer model. (**a**) In the convection-resolving model, the radiative heating profile is switched from cool-climate-type to hothouse-type (LTRH_off to LTRH_on) on model day 0 (the transient_SO simulation). (**b**) In the two-layer model, the inhibition parameter is increased linearly in time between days 0 and 2 and held fixed thereafter.

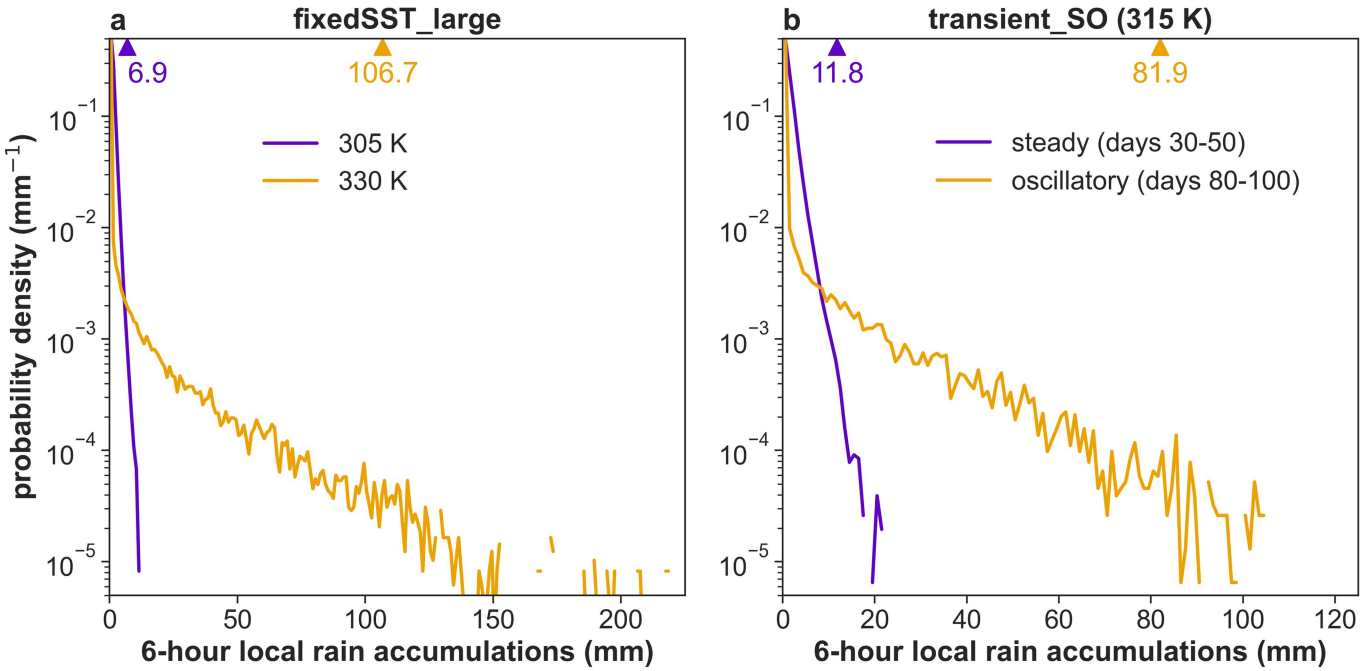

Extended Data Fig. 8 | Probability density functions (PDFs) of 6-hour local rain accumulations. The precipitation data are from 20-day periods of (**a**) the fixedSST_large simulations, and (**b**) the transient_SO simulation in the steady and oscillatory regime. The PDFs are constructed by first dividing the model domains into watershed-sized subdomains (16 × 16 km^2 for fixedSST_large, and 12 × 12 km^2 for transient_SO). Precipitation is then accumulated in each subdomain for all 6-hour periods during the 20-day intervals, producing the 6-hour local rain accumulations from which the PDFs are constructed. The 99.9th percentile of each of the PDFs is indicated at the top of each plot.

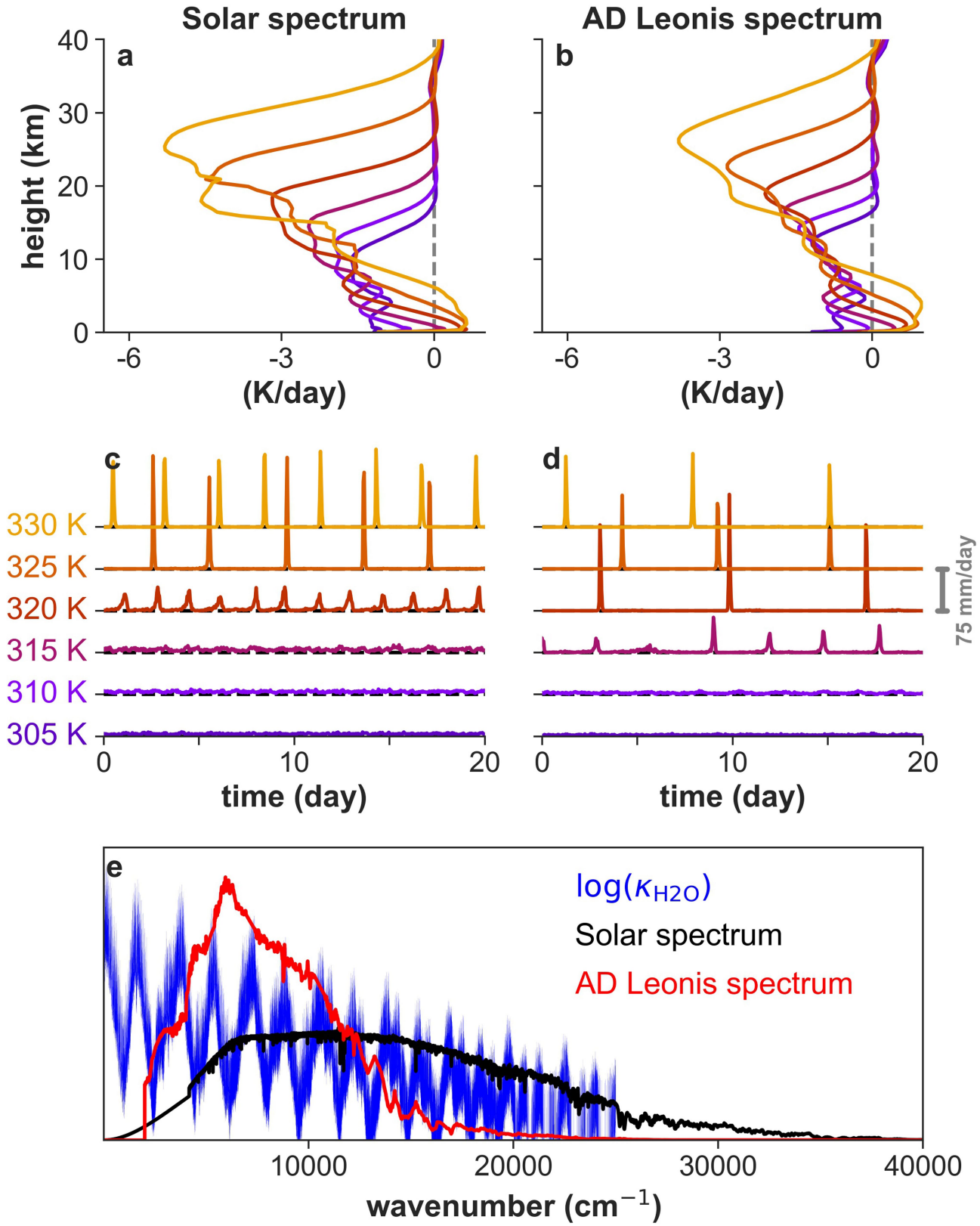

Extended Data Fig. 9 | The oscillatory transition occurs more readily for climates instellated by an M-star spectrum. Comparison of tropospheric radiative heating rates (panels **a**,**b**) and timeseries of surface precipitation (panels **c**,**d**) in fixed-SST simulations with either the solar instellation spectrum or that of the M-star AD Leonis[62]. Panel (**e**) shows the spectral flux for these two stars (normalized to the same total flux), as well as the logarithm of the H_2O absorption coefficient at a reference temperature and pressure.

Extended Data Table 1 | Summary of key aspects of the suite of DAM simulations conducted for this work

experiment name	SST(K)	radiation	duration	notes
fixedSST	305, 310, 315, 320–326 at 1-K increments, 330	interactive	200 days	-
CTRL	evolving	interactive	50 days	ocean heat sink applied
FSOL	evolving	interactive	4 years	solar constant increased by 10%, ocean heat sink applied
FCO2	evolving	interactive	4 years	CO_2 increased by 64x, ocean heat sink applied
LTRH_on	305–330 at 5-K increments	prescribed	100 days	bulk tropospheric radiative cooling matches fixedSST
LTRH_off	305–330 at 5-K increments	prescribed	100 days	bulk tropospheric radiative cooling matches fixedSST
transient_SO	315	prescribed	100 days	radiation switched from LTRH_off to LTRH_on after 50 days; larger domain (L_x = 216 km)
fixedSST_large	305, 330	interactive	50 days	larger domain (L_x = 512 km)
fixedSST_hires	305, 330	interactive	20 days	finer horizontal resolution (Δx = 250 m)
fixedSST_sm	305, 330	interactive, clear-sky	300 days	simple microphysics
prevap0	330	prescribed	300 days	evaporation of precipitating hydrometeors turned off
MSTAR	305–330 at 5-K increments	interactive, clear-sky	100 days	instellation spectrum from Ad Leonis B

For each experiment, the table lists the sea surface temperature (SST) lower boundary condition, the radiative transfer method, the duration of model integration, and additional noteworthy features.